

**The following resources related to this article are available online at [www.sciencemag.org](http://www.sciencemag.org) (this information is current as of December 7, 2009):**

**Updated information and services**, including high-resolution figures, can be found in the online version of this article at:

<http://www.sciencemag.org/cgi/content/full/312/5772/410>

A list of selected additional articles on the Science Web sites **related to this article** can be found at:

<http://www.sciencemag.org/cgi/content/full/312/5772/410#related-content>

This article **cites 27 articles**, 3 of which can be accessed for free:

<http://www.sciencemag.org/cgi/content/full/312/5772/410#otherarticles>

This article has been **cited by** 55 article(s) on the ISI Web of Science.

This article appears in the following **subject collections**:

Physics, Applied

[http://www.sciencemag.org/cgi/collection/app\\_physics](http://www.sciencemag.org/cgi/collection/app_physics)

Information about obtaining **reprints** of this article or about obtaining **permission to reproduce this article** in whole or in part can be found at:

<http://www.sciencemag.org/about/permissions.dtl>

- sulfation on the second galactose was not tolerated (no. 37) for Viet04, although binding was apparent for sialosides with Gal in either  $\beta$ 1-3 or  $\beta$ 1-4 linkage to a GlcNAc or GalNAc (nos. 21 to 23, 32, 33), as well as to fucosylated glycans (nos. 26 to 29).
39. A. Gambaryan *et al.*, *Virology* **344**, 432 (2006).
  40. H. Debray, D. Decout, G. Strecker, G. Spik, J. Montreuil, *Eur. J. Biochem.* **117**, 41 (1981).
  41. R. J. Connor, Y. Kawaoka, R. G. Webster, J. C. Paulson, *Virology* **205**, 17 (1994).
  42. G. N. Rogers *et al.*, *Nature* **304**, 76 (1983).
  43. M. Matrosovich *et al.*, *J. Virol.* **74**, 8502 (2000).
  44. E. Nobusawa, H. Ishihara, T. Morishita, K. Sato, K. Nakajima, *Virology* **278**, 587 (2000).
  45. L. Glaser *et al.*, *J. Virol.* **79**, 11533 (2005).
  46. Avian H1 bound only to nonbranched glycans and to sulfated and/or negatively charged glycans (Figs. 4C and 5, A to C). The single E190D mutation reduced binding to most  $\alpha$ 2-3 glycans, except to sulfated sialosides (Fig. 5A). These results suggest mutation at both 190 and 225 positions is always a requirement for H1 serotypes to adapt to a human host.
  47. R. A. Fouchier *et al.*, *J. Virol.* **79**, 2814 (2005).
  48. The E190D mutation (Fig. 5D) reduced overall binding of  $\alpha$ 2-3 ligands and glycoproteins, except for the sulfated and/or negatively charged glycans (nos. 18, 20, 24, 25, and 38). The G225D mutation (Fig. 5E) appeared to have little effect on the binding profile, in contrast to avian H1, where binding was not detected (Fig. 5B). The double mutant (E190D,G225D) did not bind to any glycan on the array (see Fig. 5F).
  49. S. J. Gamblin *et al.*, *Science* **303**, 1838 (2004).
  50. For the human H1 HA from A/Puerto Rico/8/1934, the longer side chain of Glu<sup>190</sup> can form hydrogen bonds to sialic acid of both  $\alpha$ 2-6 and  $\alpha$ 2-3 sialosides, whereas for structures of A/Swine/Iowa/1930, H1 HA bound to human receptor analogs, the shorter side chain of Asp<sup>190</sup> can only interact with the GlcNAc to stabilize the  $\alpha$ 2-6 conformation (49). Binding data, with the 1918 South Carolina H1 HA (35) and the Dk76 double mutation (E190D,G225D) (Fig. 5C), show that some sulfated glycans with  $\alpha$ 2-6 sialic acid linkages can bind. However, this situation does not arise for the Viet04 double mutant. Although the G225D mutation would have been expected to enhance  $\alpha$ 2-6 specificity, the additional stabilizing influence of the E190D mutation toward the GlcNAc may not be possible because of the neighboring Lys<sup>193</sup>, which could inhibit interaction of Asp<sup>190</sup> with the glycan either by steric hindrance or by direct interaction with Asp<sup>190</sup>. Experiments are in progress to test this notion.
  51. The Q226L mutation eliminated binding to the microarray, except for two negatively charged  $\alpha$ 2-3 glycans [with either an extra sialic acid on the 6-position of a GalNAc (no. 20) or 6-sulfation on GlcNAc with a branched fucose (no. 25)]. The G228S mutation did not have any significant effect compared with Viet04, except that sialosides with sulfation on the 6-position of the galactose, with or without branched fucosylation on the GlcNAc (nos. 12, 37) were tolerated. Stronger binding was observed for fucosylated glycans (nos. 26 to 29), and reduced binding was observed for sialosides with  $\beta$ 1-3 linkages between the galactose and GlcNAc/GalNAc (nos. 21 to 23) (Fig. 5H). In addition to 6'-sialyllactose (no. 49), as seen for Viet04, binding was observed for  $\alpha$ 2-6 biantennary structures (nos. 56 and 57). The double mutant (Q226L,G228S) showed reduced binding to  $\alpha$ 2-3 sialosides. Only sulfated and long-chain glycans were tolerated (nos. 16, 20, 24, 25, 35), but binding to  $\alpha$ 2-6 biantennary structures (nos. 56 and 57), as with the G228S mutation, was also maintained.
  52. R. Harvey, A. C. Martin, M. Zambon, W. S. Barclay, *J. Virol.* **78**, 502 (2004).
  53. D. H. Joziase *et al.*, *J. Biol. Chem.* **262**, 2025 (1987).
  54. See glycan structure database ([www.functionalglycomics.org](http://www.functionalglycomics.org)).
  55. L. G. Baum, J. C. Paulson, *Acta Histochem. Suppl.* **40**, 35 (1990).
  56. P. Gagneux *et al.*, *J. Biol. Chem.* **278**, 48245 (2003).
  57. M. N. Matrosovich, T. Y. Matrosovich, T. Gray, N. A. Roberts, H. D. Klenk, *Proc. Natl. Acad. Sci. U.S.A.* **101**, 4620 (2004).
  58. G. Lamblin *et al.*, *Glycoconj. J.* **18**, 661 (2001).
  59. Attenuated viruses with a S227N mutation led to higher hemagglutinin inhibition titers in ferrets (60). Thus, enhanced binding to  $\alpha$ 2-3 ligands, especially to 6-sulfated GalNAc, could lead to an increased uptake into antigen-presenting cells and subsequent antibody production.
  60. E. Hoffmann, A. S. Lipatov, R. J. Webby, E. A. Govorkova, R. G. Webster, *Proc. Natl. Acad. Sci. U.S.A.* **102**, 12915 (2005).
  61. The 2003 isolates contain Ala<sup>160</sup>, Arg<sup>193</sup>, Lys<sup>216</sup> and Asn<sup>227</sup>, whereas Viet04 has Thr<sup>160</sup> (which introduces a glycosylation site at Asn<sup>158</sup>), Lys<sup>193</sup>, Arg<sup>216</sup>, and Ser<sup>227</sup>.
  62. Consortium for Functional Glycomics ([www.functionalglycomics.org](http://www.functionalglycomics.org)).
  63. H. D. Klenk, R. Wagner, D. Heuer, T. Wolff, *Virus Res.* **82**, 73 (2002).
  64. T. A. Kost, J. P. Condeary, D. L. Jarvis, *Nat. Biotechnol.* **23**, 567 (2005).
  65. G. N. Rogers, J. C. Paulson, *Virology* **127**, 361 (1983).
  66. W. L. Delano (2002); ([www.pymol.org](http://www.pymol.org)).
  67. The work was supported in part by National Institute of Allergy and Infectious Diseases grant AI058113 (I.A.W., T.T., J.K.T.); National Institute of General Medical Sciences grants GM062116 (to J.C.P., I.A.W.) and GM060938 (to J.C.P.); and partial support from NIH grants to I.A.W. (CA55896 and AI42266). We thank P. Palese and L. Glaser (Mount Sinai School of Medicine, New York) for providing the full-length clone of A/Vietnam/1203/2004; the staff of the Advanced Light Source Beamline 8.2.2 for the beamline assistance; X. Dai, S. Ferguson, P. Carney, and J. Vanhansy (The Scripps Research Institute) for expert technical assistance; and R. Stanfield and M. Elsliger (The Scripps Research Institute) for helpful discussions. This is publication 17916-MB from The Scripps Research Institute. Coordinates and structure factors have been deposited in the Protein Data Bank (code 2FK0) and will be released on publication.

#### Supporting Online Material

[www.sciencemag.org/cgi/content/full/1124513/DC1](http://www.sciencemag.org/cgi/content/full/1124513/DC1)  
Materials and Methods  
Figs. S1 to S6  
Tables S1 to S4  
References

3 January 2006; accepted 28 February 2006  
Published online 16 March 2006;  
10.1126/science.1124513  
Include this information when citing this paper.

## REPORTS

# Ultrafast Laser-Driven Microlens to Focus and Energy-Select Mega-Electron Volt Protons

Toma Toncian,<sup>1</sup> Marco Borghesi,<sup>2</sup> Julien Fuchs,<sup>3</sup> Emmanuel d'Humières,<sup>3,4</sup> Patrizio Antici,<sup>3</sup> Patrick Audebert,<sup>3</sup> Erik Brambrink,<sup>3</sup> Carlo Alberto Cecchetti,<sup>2</sup> Ariane Pipahl,<sup>1</sup> Lorenzo Romagnani,<sup>2</sup> Oswald Willi<sup>1\*</sup>

We present a technique for simultaneous focusing and energy selection of high-current, mega-electron volt proton beams with the use of radial, transient electric fields ( $10^7$  to  $10^{10}$  volts per meter) triggered on the inner walls of a hollow microcylinder by an intense subpicosecond laser pulse. Because of the transient nature of the focusing fields, the proposed method allows selection of a desired range out of the spectrum of the polyenergetic proton beam. This technique addresses current drawbacks of laser-accelerated proton beams, such as their broad spectrum and divergence at the source.

The recent development of ultra-intense laser pulses (1) has opened up opportunities for applications in many areas, including particle acceleration (2–5), inertial fusion energy (6), generation of intense x-ray

pulses (7), laser-driven nuclear physics (8), and laboratory astrophysics (9). In particular, the acceleration of mega-electron volt ions from the interaction of high-intensity laser-pulses with thin solids has major applicative prospects

because of the high beam quality of these ion bursts (10, 11). Such proton beams are already applied to produce high-energy density matter (12) or to radiograph transient processes (13), and they offer promising prospects for tumor therapy (14), isotope generation for positron emission tomography (15), fast ignition of fusion cores (16), and brightness increase of conventional accelerators. However, because these proton beams are polyenergetic and divergent at the source, reduction and control of their divergence and energy spread are essential requirements for most of these applications.

<sup>1</sup>Heinrich Heine Universität Düsseldorf, D-40225 Düsseldorf, Germany. <sup>2</sup>School of Mathematics and Physics, The Queen's University of Belfast, Belfast BT7 1NN, Northern Ireland, UK. <sup>3</sup>Laboratoire pour l'Utilisation des Lasers Intenses, UMR 7605 CNRS-CEA-Ecole Polytechnique-Université Paris VI, 91128 Palaiseau, France. <sup>4</sup>Centre de Physique Théorique, UMR 7644 CNRS-Ecole Polytechnique, 91128 Palaiseau, France.

\*To whom correspondence should be addressed. E-mail: [oswald.willi@laserphy.uni-duesseldorf.de](mailto:oswald.willi@laserphy.uni-duesseldorf.de)

Focusing of energetic proton beams is usually achieved with electrostatic or magnetic lenses (17), which have several drawbacks, including slow switching times, large sizes, asymmetry in the transverse plane for the focused beam, aberrations, inability to focus large currents, and large heat dissipation. It has been proposed that particle selection and beam collimation of laser-produced protons applicable for tumor therapy could be achieved by means of superconducting magnet systems (18). Relativistic laser-plasma devices appear in principle more suitable for achieving the required angular and spectral control of laser-accelerated ion beams because they can withstand large ion beam currents, can be switched over picosecond time scales, and can support large deflecting fields on microscales.

Advances in ion beam tailoring have been achieved so far mainly with the use of target engineering techniques. Geometrical focusing of laser-driven protons has been attained with the use of curved targets (12). Demonstration of this technique has been limited so far to focal distances of a few millimeters and to the low-energy component of the proton spectrum. Very recently, quasi-monochromatic acceleration from laser irradiated microstructured targets has been reported (19, 20). In these approaches, the focusing or energy-selection effect is achieved by directly acting on the source. As a consequence, these techniques rely on relatively complex target fabrication or preparation procedures.

We describe here an alternative approach, which provides tunable, simultaneous focusing and energy selection of mega-electron volt proton beams. Furthermore, our approach decouples the beam tailoring stage from the acceleration stage, allowing for their independent optimization. This leads to a system with higher flexibility than the methods above, considerably relaxing the target fabrication constraints. The method uses a compact laser-driven microlens arrangement (Fig. 1A). The underlying physical process begins with relativistic electrons injected through the cylinder's wall produced by the laser operating in chirped pulse amplification (CPA) mode, which spread evenly on the cylinder's inner walls and initiate hot plasma expansion (Fig. 1, B and C). The transient electric fields associated with the expansion are used in a radial geometry to focus protons accelerated by a separate CPA laser pulse from a thin planar foil. The microlens operation was demonstrated in experiments carried out at the Laboratoire pour l'Utilisation des Lasers Intenses (LULI), which used the 100-TW laser (21) operating at a wavelength of 1  $\mu\text{m}$ . After amplification, the laser pulse was split into two separate pulses (CPA<sub>1</sub> and CPA<sub>2</sub>), which were recompressed in separate grating compressors to a 350-fs duration. The delay between the two pulses was controlled optically with picosecond precision. The CPA<sub>1</sub> pulse (irradiance  $I = 5 \times 10^{19} \text{ W/cm}^2$ ) was used

to accelerate a high-current, diverging beam of up to 15-MeV protons from a 25- $\mu\text{m}$ -thick Al foil target [the protons are produced from hydrocarbon impurities (22) on the target rear surface (23, 24)]. The CPA<sub>2</sub> pulse ( $I = 3 \times 10^{18} \text{ W/cm}^2$ ) was focused onto the outer wall of a hollow cylinder. The proton beam from the first foil was directed through the cylinder and detected with a stack of radiochromic films (RCF), a dosimetric detector (25), positioned at a variable distance (from 2 to 70 cm) from the proton source. The RCF stack was used to measure the proton beam divergence. It also provided a coarse energy resolution due to the energy deposition properties of the ions (3) (most of the energy of a proton is released in the so-called Bragg peak, located at a distance in the detector which depends on the incident proton energy). It was shielded with an 11- $\mu\text{m}$  Al foil allowing protons with energies greater than 1.5 MeV to be recorded. In some cases, a central millimeter-sized hole was bored through the RCF to allow downstream high spectral resolution measurements with the use of a magnetic spectrometer with a 0.6-T permanent magnet. The spectral resolution determined by the slit width and the dispersion of the spectrometer is 0.2 MeV at 6 MeV and 0.7 MeV at 15 MeV. The distance between the proton production foil and cylinder and the distance between the cylinder and detector were varied throughout the experiment. At a source-cylinder distance of 1 mm, the proton flux increase due to focusing by the microlens

was so strong that saturation of the film occurred. Quantitative data could only be obtained when the cylinder was moved to 4 mm from the proton foil, in order to collect a smaller part of the diverging proton beam.

An RCF pack placed 9.5 cm away from the proton target recorded the proton beam after its propagation through a laser-irradiated dural cylinder 3 mm in length, 700  $\mu\text{m}$  in diameter, and 50  $\mu\text{m}$  in wall thickness. The fifth and sixth in the stack, corresponding to protons of 9 and 7.5 MeV, respectively, are shown in Fig. 2A. The entrance plane of the cylinder was placed 4 mm from the proton-producing foil. The distance from the proton-producing foil to the CPA<sub>2</sub> irradiation point on the cylinder was 5 mm. As expected, no focusing effect is observed for the 9 MeV protons. Indeed, the electric field is triggered by the CPA<sub>2</sub> laser pulse  $\sim 20$  ps after these protons exit the cylinder. For the 7.5-MeV protons, the electric field develops while these protons are close to exit the cylinder, and a small spot about 600  $\mu\text{m}$  [full width at half

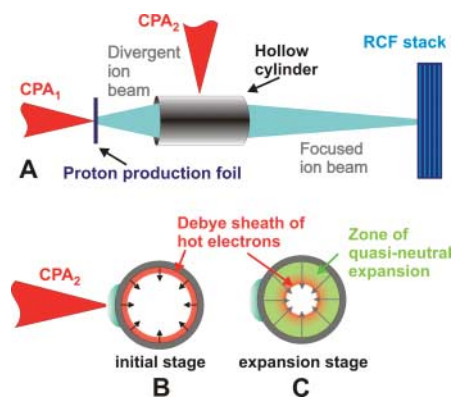


**Fig. 1.** (A) Schematic of the microlens device. A proton beam is accelerated from a planar foil by the CPA<sub>1</sub> laser pulse. The proton beam propagates through a hollow cylinder side irradiated by the CPA<sub>2</sub> laser pulse. (B and C) Schematic of the operation's principle of the microlens. The CPA<sub>2</sub> laser pulse injects hot electrons within the cylinder. These spread evenly onto the cylinder's inner wall. In the early stage (B), these electrons, confined over a Debye length on the cylinder's surface, generate a space-charge field (indicated by the radially pointing arrows), which then induces plasma expansion (C) from the cylinder's inner walls. The resulting radial electric field, still indicated by the arrows and decreasing in time as the plasma expands, focuses the protons. The field is peaked at the front but extends toward the cylinder's wall.

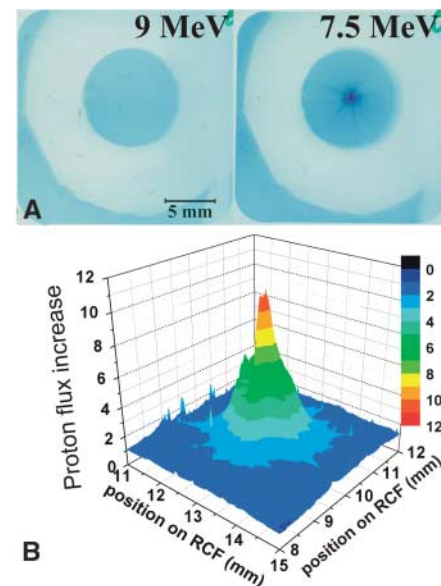


**Fig. 2.** (A) RCF layers showing the proton beam focusing effect due to a 3-mm-long, 700- $\mu\text{m}$ -diameter dural (95% Al, 4% Cu, and 1% Mg) laser-irradiated cylinder with 50- $\mu\text{m}$  wall thickness. For the energies reaching the Bragg peak in the two layers shown, the protons with an energy of 9 MeV pass through the cylinder before the electric field is present, showing no focusing, whereas the divergence of the protons with an energy of 7.5 MeV is strongly reduced by the electric field that has developed inside the cylinder. The shadow of the cylinder and of the 50- $\mu\text{m}$  tungsten holding wire can be seen clearly. The cylinder was positioned far from the proton source intentionally to reduce the number of protons entering the cylinder and avoid RCF saturation. The distance between the entrance plane of the cylinder and the proton production foil was 4 mm. (B) Flux increase with respect to the unfocused flux for 7.5-MeV protons as deduced from the layer shown in (A).

maximum (FWHM)] in diameter is seen on the RCF at the center of the cylinder's shadow (spots as small as 200  $\mu\text{m}$  have been observed, depending on the detector position). In this case, the proton flux within the spot at the film plane is increased as many as 12 times compared with the unfocused part not captured by the cylinder (Fig. 2B). Based on the known properties of the proton source and on the decay time of the focusing fields [inferred to be  $\sim 10$  ps from particle-in-cell (PIC) simulations and experimental results (26)], a focused current of about 5 A can be estimated for the conditions of Fig. 3. We also studied the evolution of the beam size, as a function of the propagation distance from the cylinder. This was done under the same conditions of Fig. 2. The behavior of the 7.5-MeV proton component is shown in Fig. 3. For this energy, the beam size is only 8 mm after 70 cm of propagation, whereas when freely propagating, the size of the beam would have been  $\sim 260$  mm. An energy spectrum was obtained, in the same experimental configuration, with the use of the magnetic spectrometer, having an entrance slit of 250  $\mu\text{m}$  positioned 70 cm away from the proton source (Fig. 4). As a reference, we also show a typical exponential spectrum collected in the same conditions but without the microlens. The data clearly shows the energy-selection capability of the microlens: Because of selective collimation of the 6.25-MeV protons, these could be transmitted efficiently through the spectrometer slit (acting as an angular filter), and their density after the slit in the spectrally dispersed plane is enhanced as compared with the free-space expansion case. For this shot, the 6.25-MeV protons experience the focusing fields for

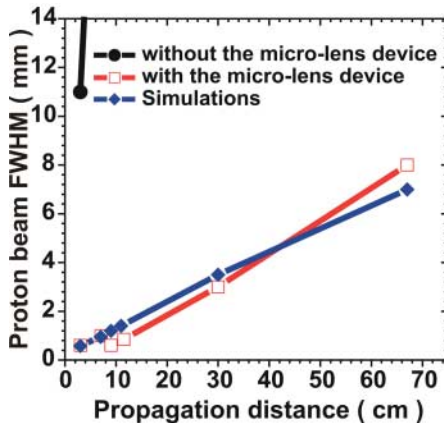


**Fig. 3.** Evolution of the FWHM of the proton beam along its propagation, for protons with energy of 7.5 MeV (the propagation distance is calculated from the proton source). The black circles correspond to the case without the microlens (free-space divergence), the blue diamonds to the particle-tracer simulation in the fields given by the PIC simulation, and the red squares to the experimental results with the use of the microlens. The RCF shown on the right of Fig. 2A corresponds to the red point at 9.5 cm.

$\sim 5$  ps before exiting the cylinder. We obtained an energy spread of 0.2 MeV—limited by the spectrometer energy resolution—for the peak located at 6.25 MeV. The numerical simulations performed in the same conditions as in the experiment suggest that the spectral width of the peak is about 0.1 MeV and hence narrower than demonstrated by the experimental spectrum shown (Fig. 4). By varying the optical delay between the laser beams, the location of this peak on the energy axis can be tuned selectively (as demonstrated experimentally), thereby allowing us to tailor the energy distribution of the transmitted beam, a necessary step for many applications. Notably, with this approach, focusing and energy selection are provided simultaneously.

We performed one-dimensional (1D) and 2D PIC simulations of field generation at the microlens's walls and 3D test-particle simulations of proton propagation through the microlens. The simulations were performed in three steps with the use of the CALDER code (27). First, we verified with 2D simulations that the laser pulse triggering the microlens by irradiating the cylinder's outer wall generated a population of hot electrons that spread evenly on the cylinder's walls. We then used a 1D code to simulate the plasma expansion within the cylinder (i.e., we simulated the expansion of two slabs of plasma separated by the cylinder's diameter of 700  $\mu\text{m}$ ). The expansion is driven by a hot-electron population that has a Boltzmann distribution with a temperature of 400 keV, as given by the ponderomotive potential at the irradiance of CPA<sub>2</sub> (28). The initial electron density at the cylinder's wall was estimated by considering that a 40% fraction of the laser energy [inferred

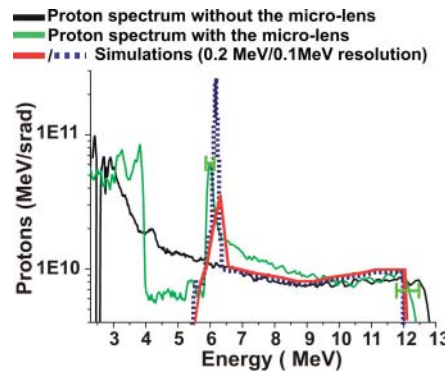


**Fig. 4.** Experimental proton spectra measured with a magnetic spectrometer without the microlens (black line) and with the microlens (green line), and proton spectra obtained from simulations (red and blue lines) performed with the use of the experimental proton beam parameters and the magnetic spectrometer parameters (i.e., distance from the source and slit characteristics). The red and blue curves were obtained with the use of energy bins of 0.2 and 0.1 MeV, respectively. The simulated spectrum was obtained by tracing, for each energy bin, 5000 protons through the fields predicted by the PIC simulation.

from experimental measurements (29)] is converted into hot electrons and that these are then spread evenly on the cylinder's walls. This results in a hot-electron density of  $\sim 6 \times 10^{16} \text{ cm}^{-3}$ . We assumed that when the plasma expansion starts, the field obtained in the PIC simulation is the same along the whole cylinder. Finally, we simulated the propagation of a proton beam in the cylinder through the space- and time-dependent fields obtained from the PIC simulation. The proton source used in the simulations has a divergence and energy spectrum as measured in the experiment.

The successful comparison between the simulations and the data (Figs. 3 and 4) supports the scenario in which laser-triggered transient fields drive the selective deflection of the protons. The transient field (30) is associated with a hot-electron sheath that extends over a Debye length ahead of the plasma, expanding toward the cylinder's axis (26, 31). The different energy components present in the proton beam spectrum transit through the cylinder at different times depending on their different velocities, with higher energy protons crossing the cylinder at earlier times. Protons passing through the microlens before it is triggered (as in Fig. 2A for the 9-MeV layer) do not experience any fields and are therefore not deflected. Protons which are crossing the cylinder and are close to its end when it is triggered and that therefore experience the fields for only a short time will exit the cylinder with a very low divergence (as in Fig. 2A for the 7.5-MeV layer). Lower energy protons will experience a larger cumulated field along their propagation through the cylinder. The particle-tracing simulations suggest that they are therefore focused at a short distance from the exit plane of the microlens and diverge strongly after focus. This is consistent with the diluted beam observed on the RCF stack positioned a few centimeters away and with the strong dip observed in the spectrum of Fig. 4 below 6 MeV. Finally, protons that have very low energy (i.e., below 4 MeV in the case of Fig. 4) pass through the microlens after the fields have vanished and do not experience any deflection. Additional simulations were performed to test the scalability of the microlens to higher proton energies, as needed for applications such as proton therapy. We computed that, using the same cylinder as in our experiment and a slightly more intense CPA<sub>2</sub> triggering laser pulse ( $10^{19} \text{ W/cm}^2$ ), one could reduce the divergence of 270-MeV protons. Protons of such high energy transit through the microlens in a short time (13 ps); therefore, even higher laser intensities, on the order of  $10^{20} \text{ W/cm}^2$ , would be required to focus them. The focusing device described in this paper has potential use in all applications of energetic protons in which reduced divergence, large flux, or narrow energy range are required. These include most of the proposed applications in scientific, medical, and technological areas. For

example, focusing ion beams provides a different perspective, which may lead to further developments in areas such as hadron therapy for cancer treatment, accelerator physics, and inertial fusion physics. In addition to applications that use laser-driven ion beams, such a device might find application in conventional accelerator beams as a focusing or fast-switching tool.

#### References and Notes

- M. D. Perry, G. Mourou, *Science* **264**, 917 (1994).
- E. Clark *et al.*, *Phys. Rev. Lett.* **84**, 670 (2000).
- R. Snavely *et al.*, *Phys. Rev. Lett.* **85**, 2945 (2000).
- A. Maksimchuk, S. Gu, K. Flippo, D. Umstadter, V. Yu. Bychenkov, *Phys. Rev. Lett.* **84**, 4108 (2000).
- V. Malka, J. Faure, Y. Glinec, A. F. Lifschitz, *Plasma Phys. Control. Fusion* **47**, B481 (2005).
- M. Tabak *et al.*, *Phys. Plasmas* **1**, 1626 (1994).
- A. Rousse *et al.*, *Phys. Rev. Lett.* **93**, 135005 (2004).
- K. W. D. Ledingham, P. McKenna, R. P. Shinghal, *Science* **300**, 1107 (2003).
- B. A. Remington, D. Arnet, R. P. Drake, H. Takabe, *Science* **284**, 1488 (1999).
- M. Borghesi *et al.*, *Phys. Rev. Lett.* **92**, 055003 (2004).
- T. Cowan *et al.*, *Phys. Rev. Lett.* **92**, 204801 (2004).
- P. Patel *et al.*, *Phys. Rev. Lett.* **91**, 125004 (2003).
- M. Borghesi *et al.*, *Phys. Plasmas* **9**, 2214 (2002).
- S. V. Bulanov, T. Zh. Esirkepov, V. S. Khoroshkov, A. V. Kuznetsov, F. Pegoraro, *Phys. Lett. A* **299**, 240 (2002).
- I. Spencer *et al.*, *Nucl. Inst. Meth. Phys. Res. B* **183**, 449 (2001).
- M. Roth *et al.*, *Phys. Rev. Lett.* **86**, 436 (2001).
- M. Szilagy, *Electron and Ion Optics* (Plenum Press, New York, 1988).
- W. Luo, E. Fourkal, J. Li, Ch. Ma, *Med. Phys.* **32**, 794 (2005).
- B. M. Hegelich *et al.*, *Nature* **439**, 441 (2006).
- H. Schwöerer *et al.*, *Nature* **439**, 445 (2006).
- B. Wattellier *et al.*, *Opt. Lett.* **29**, 2494 (2004).
- S. J. Gitomer *et al.*, *Phys. Fluids* **29**, 2679 (1986).
- M. Allen *et al.*, *Phys. Rev. Lett.* **93**, 265004 (2004).
- J. Fuchs *et al.*, *Phys. Rev. Lett.* **94**, 045004 (2005).
- GAFCHROMIC radiochromic dosimetry films ([www.ispcorp.com/products/dosimetry/index.html](http://www.ispcorp.com/products/dosimetry/index.html)).
- L. Romagnani *et al.*, *Phys. Rev. Lett.* **95**, 195001 (2005).
- E. Lefebvre *et al.*, *Nucl. Fusion* **43**, 629 (2003).
- S. C. Wilks *et al.*, *Phys. Plasmas* **8**, 542 (2001).
- M. Key *et al.*, *Phys. Plasmas* **5**, 1966 (1998).
- These fields have been studied in detail, in planar geometry, in a previous experiment (26) and figure 3 of reference (26) shows their spatial and temporal evolution.
- S. Gordienko, A. Pukhov, personal communication.
- We thank L. Gremillet, T. Grismayer, S. Gordienko, E. Lefebvre, P. Mora, A. Pukhov, and V. Malka for fruitful discussions; E. Lefebvre for allowing us to use his PIC code CALDER; and the Commissariat à l'Énergie Atomique/Direction des Applications Militaires (CEA/DAM) for the simulations we performed on Le Centre de Calcul Recherche et Technologie (CCRT) computers. We acknowledge the support from the technical teams at LULI. This work was supported by European Union grant no. HPRIC1999-0052, grant no. E1127 from Région Ile-de-France, and DFG TR18 and GK1203, and partly by the Queen's University of Belfast-International Research Centre for Experimental Physics (QUB-IRCEP) Distinguished Fellowship Visiting scheme and Deutscher Akademischer Austausch Dienst (DAAD).

28 December 2005; accepted 9 February 2006

Published online 16 February 2006;

10.1126/science.1124412

Include this information when citing this paper.

# Bolometric Infrared Photoresponse of Suspended Single-Walled Carbon Nanotube Films

Mikhail E. Itkis, Ferenc Borondics,\* Aiping Yu, Robert C. Haddon†

The photoresponse in the electrical conductivity of a single-walled carbon nanotube (SWNT) film is dramatically enhanced when the nanotube film is suspended in vacuum. We show here that the change in conductivity is bolometric (caused by heating of the SWNT network). Electron-phonon interactions lead to ultrafast relaxation of the photoexcited carriers, and the energy of the incident infrared (IR) radiation is efficiently transferred to the crystal lattice. It is not the presence of photoexcited holes and electrons, but a rise in temperature, that results in a change in resistance; thus, photoconductivity experiments cannot be used to support the band picture over the exciton model of excited states in carbon nanotubes. The photoresponse of suspended SWNT films is sufficiently high that they may function as the sensitive element of an IR bolometric detector.

The optical properties of SWNTs, including photoconductivity, suggest outstanding potential for applications in nanoscale-sized optoelectronics (1–4). Prominent absorption features in the optical spectra of SWNTs have been widely ascribed to interband transitions associated with the series of van Hove singularities in the one-dimensional (1D) electronic density of states (5–7). However, more-recent studies suggest that the electron-hole pairs are strongly coupled in the SWNT 1D crystal lattice and that major photoexcitations are excitons, rather than free carriers (8–11). Experiments on the relaxation of photoexcitations in SWNTs (11) and two-photon excitation spec-

troscopy (12) support the exciton model and provide a large value for the exciton binding energy (0.4 eV) (12).

In the interband transition (band) model, free electrons and holes are produced upon photoexcitation, and, providing the lifetime of these carriers is sufficiently long, the spectral features in absorption and photoconductivity match the optical transitions associated with the van Hove singularities (Fig. 1A). In the exciton model, the photoexcitations occur at energies lower than the direct bandgap and give rise to neutral species that cannot directly contribute to the photoconductivity (Fig. 1A). In this situation, the excitons would have to be dissociated thermally (13) or by a large electric field (12) to produce free electrons and holes that could contribute to the photoconductivity. Exciton-related low-energy spectral features in the photoresponse would be substantially suppressed, especially at low temperatures, compared with the features corresponding to the interband transitions, and differences should arise in the absorption and photoconductivity spectra.

There are a number of reports on the photoconductivity of SWNT films deposited on optical substrates (13–15). In all cases, a very weak photoresponse with low signal-to-noise (S/N) ratio was observed despite the use of high laser powers. Nevertheless, the photoconductivity showed spectral features that coincided with the optical absorption spectrum in support of the original band model, with free carriers as the major photoexcitations (13–15). Recent photoconductivity experiments on individual SWNTs (laser power intensity of 1 kW/cm<sup>2</sup>) in a field-effect-transistor configuration gave a weak sideband in addition to the primary resonance, and the result was interpreted in a favor of the exciton model (16).

We report here on the photoconductivity of suspended SWNT films, and we are able to rationalize contradictory reports to date, as well as shed light on the nature of the optical excitations in SWNTs and the origin of the photoresponse. The extremely large photoresponse that is observed for suspended SWNT films also makes them attractive candidates for the sensitive element of an infrared (IR) bolometer.

Photoconductivity experiments were carried out with semitransparent SWNT films prepared by two different techniques. A network of as-prepared (AP) SWNTs can form in the electric arc discharge process. The network growth was initiated by the placement of stainless steel wire grids of cell size 2.54 × 2.54 cm near the plasma zone inside the electric arc chamber. The growing SWNTs drift from the plasma core toward the water-cooled walls of the arc reactor, and the wire grid nucleates the growth of an extended SWNT network that forms a continuous semitransparent SWNT film after 1 to 5 min of operation of the electric arc (fig. S1). This process leads to a high-purity film, because the SWNTs are trapped in the growing network with high probability; but typical impurities, such as nanoparticles and amorphous carbon, penetrate the thin network without becoming entangled. We

Center for Nanoscale Science and Engineering, Departments of Chemistry and Chemical and Environmental Engineering, University of California, Riverside, CA 92521-0403, USA.

\*Present address: Magyar Tudományos Akadémia, Szilárdtestfizikai és Optikai Kutatóintézete, Budapest, H 1525, Hungary.

†To whom correspondence should be addressed. E-mail: haddon@ucr.edu